HHS Public Access

Author manuscript

J Am Chem Soc. Author manuscript; available in PMC 2023 March 13.

Published in final edited form as:

J Am Chem Soc. 2022 December 28; 144(51): 23668–23676. doi:10.1021/jacs.2c11223.

Photostable Small-Molecule NIR-II Fluorescent Scaffolds that Cross the Blood-Brain Barrier for Noninvasive Brain Imaging

Shichao Wang[a,†], **Hui Shi**[b,c,†], **Lushun Wang**[a], **Axel Loredo**[a], **Sergei M. Bachilo**[a], **William Wu**[a], **Zeru Tian**[a], **Yuda Chen**[a], **R. Bruce Weisman**[a], **Xuanjun Zhang**[d], **Zhen Cheng**[b,c,e,*], **Han Xiao**[a,f,g,*]

[a]Department of Chemistry, Rice University, 6100 Main Street, Houston, Texas, 77005, USA

[b]State Key Laboratory of Drug Research, Molecular Imaging Center, Shanghai Institute of Materia Medica, Chinese Academy of Sciences, Shanghai, 201203, China

[c]Molecular Imaging Program at Stanford (MIPS), Department of Radiology and Bio-X Program, Stanford University, Stanford, CA 94305, USA

[d]MOE Frontiers Science Center for Precision Oncology, Faculty of Health Sciences, University of Macau, Macau SAR, 999078, China

[e]Shandong Laboratory of Yantai Drug Discovery, Bohai Rim Advanced Research Institute for Drug Discovery, Yantai, Shandong 264117, China

[f]Department of Biosciences, Rice University, 6100 Main Street, Houston, Texas, 77005, USA

[g]Department of Bioengineering, Rice University, 6100 Main Street, Houston, Texas, 77005, USA

Abstract

The second near-infrared (NIR-II, 1000–1700 nm) fluorescent probes have significant advantages over visible or NIR-I (600–900 nm) imaging for both depth of penetration and level of resolution. Since the blood-brain barrier (BBB) prevents most molecules from entering the central nervous system, NIR-II dyes with large molecular frameworks have limited applications for brain imaging. In this work, we developed a series of boron difluoride (BF_2) formazanate NIR-II dyes which had tunable photophysical properties, ultrahigh photostability, excellent biological stability, and strong brightness. Modulation of the aniline moiety of BF_2 formazanate dyes significantly enhances their abilities to cross the BBB for noninvasive brain imaging. Furthermore, the intact mouse brain imaging and dynamic BBB diffusion were monitored using these BF_2 formazanate dyes in the NIR-II region. In murine glioblastoma models, these dyes can differentiate tumors from normal brain tissues. We anticipate that this new type of small molecule will find potential applications in creating probes and drugs relevant to theranostic for brain pathologies.

*Corresponding Author: zcheng@simm.ac.cn (Zhen Cheng) han.xiao@rice.edu (Han Xiao).
†These authors contributed equally.

The authors declare no competing financial interests.

ASSOCIATED CONTENT

Supporting Information

The Supporting Information is available free of charge on the ACS Publications website. brief description (file type, i.e., PDF) brief description (file type, i.e., PDF)

Graphical Abstract

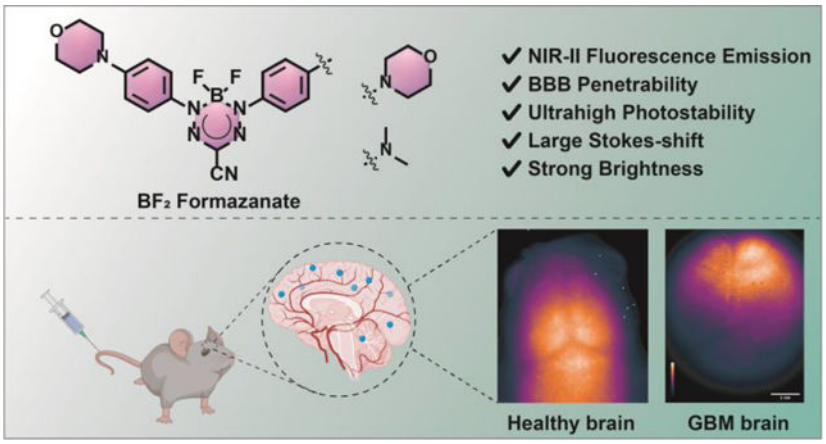

INTRODUCTION

The brain is a complex organ that represents the center of nervous system activity in mammals. Conventional imaging techniques for studying brain structure and activity include magnetic resonance imaging, positron emission tomography, computed tomography, and ultrasound imaging.[1–6] Fluorescence brain imaging is particularly attractive because of its high temporal and spatial resolution coupled with its noninvasive and in situ real-time imaging capabilities. Despite these advantages, fluorescence imaging *in vivo* has been hampered for light microscopy in the visible spectrum (400–700 nm in wavelength) by poor penetration of photons into deep tissues. Because of decreased photon scattering and reduced autofluorescence, optical bioimaging in the second near-infrared (NIR-II) channel (1000–1700 nm) is of special interest for deep-tissue imaging.[7–13] Recent studies have indicated that NIR-II probes provide high-resolution bioimaging with deeper penetration (> 9 mm depth) than conventional visible or NIR-I probes (2 mm depth).[14,15] Furthermore, the clinical utility of NIR-II biomedical imaging probes has been recently explored in human subjects.[16,17] Both nanomaterials[18–24] and small-molecule contrast agents[25–28] have been developed for performing fluorescence imaging in the NIR-II window. In contrast to nanoparticles, small molecule NIR-II fluorophores have the advantage of providing well-defined structures, tunable emission wavelengths, adjustable photophysical properties, low toxicity, and rapid metabolism.[29] Indocyanine green (ICG) is the first fluorophore in the near-infrared (NIR) region approved by the FDA for use as an intravenously administered contrast agent.[30,31] Because of its tail emission in the NIR-II region, ICG was recently used for NIR-II fluorescence imaging in vivo.[32–34] Furthermore, ICG-based NIR-II imaging has been recently explored in human cancer patients and shows that NIR-II imaging has significantly clinical advantages such as higher imaging contrast, resolution, and diseases detection sensitivity compared to NIR-I imaging.[16] In addition to ICG, several other types of small molecule NIR-II dyes have been reported, including polymethine, benzobisthiadiazole, and dipyrromethene boron difluoride NIR-II fluorophores (Scheme 1a).[25,35–37] However, despite their success in NIR-II imaging, small-molecule NIR-II dyes capable of crossing the blood-brain barrier (BBB) are currently unavailable.

To construct an ideal small-molecule NIR-II fluorophore for brain imaging, several factors must be taken into consideration, including stability, fluorescence emission wavelength, signal strength, and molecular size. The latter factor is crucial, as evidenced by the fact that fewer than 2% of all US Food and Drug Agency (FDA)-approved small molecule drugs are able to cross the intact BBB. Quantitative structure-activity relationship studies suggest that several key physicochemical parameters, including molecular weight, lipophilicity, polar surface area, hydrogen bonding, and charge, influence the BBB permeability of molecules.[38–41]

Boron difluoride (BF_2) complexes bearing *N*-bidentate ligands have been used as probes for cell imaging and analyte sensing.[42] BF_2 complexes containing dipyrromethene ligands (BODIPYs) are most popular in this respect due to their high biocompatibility, tunable photophysical properties, and potentially high emission quantum yields. Recently, a new class of BF_2 formazanate complexes that possess tunable spectroscopic and electrochemical properties has been reported.[42–45] Similar to BODIPY dyes, formazanate dyes are comprised of a BF_2 moiety bound to a stable six-membered *N*-bidentate ligand. Joe's group has made a great contribution to the modification of BF_2 formazanate substituent groups to tune their redox activities. They found that the modification of the aniline in the BF_2 formazanate framework can significantly affect its electrochemiluminescence and photoluminescence.[46,47] Based on their work, aniline modification of BF_2 formazanates is likely to be a promising strategy to modulate their molecular polarity, fluorescence emission, and BBB penetrability for noninvasive NIR-II imaging.

In this work, by modifying the aniline moiety of BF_2 formazanates, we developed a series of NIR-II fluorophores that possess relatively small molecular weights, log *P* values between 1 and 3, and low polar surfaces, fulfilling most of Lipinski's Rules for central nervous system drug design (Scheme 1b). After modification of BF_2 formazanate fluorophores with different electron-donating groups, the dyes exhibit desirable NIR-II emission spectra in fetal bovine serum (FBS) and dimethyl sulfoxide (DMSO). This type of dyes demonstrated ultrahigh photostability, large Stokes Shift, and strong brightness. Furthermore, *in vitro* and *in vivo* experiments establish that several of these dyes penetrate the BBB efficiently, allowing for their use in noninvasive NIR-II fluorescence-based brain imaging. The ability of these dyes to differentiates normal brain tissue from glioblastoma (GBM) tissue establishes their potential use in NIR-II imaging of brain tissue and abnormalities.

RESULTS AND DISCUSSION

Design and Characterization of NIR-II BF_2 Formazanate Dyes

BF_2 formazanate fluorophores possess rich photophysical properties owing to their highly delocalized π-systems and low-lying frontier orbitals that stabilize otherwise labile radicals.[42] Most importantly, they have relatively small sizes, moderate lipophilicity, low polar surface area, and low charge, allowing for potentially high BBB permeability. In this work, a series of BF_2 formazanate fluorophores was designed with the aim to develop dyes with the emissions in the NIR-II region and the ability to cross the BBB (Figure 1a). Initially, the density-functional theory (DFT) calculations on these BF_2 formazanate fluorophores suggested that both the highest occupied molecular orbital (HOMO) and the

lowest unoccupied molecular orbital (LUMO) were mainly centered on the BF_2 formazanate backbones, with additional contributions from the π-conjugated aromatic *N*-1,3 position substituents (Figure 1b). We therefore altered the electron-rich *π*-conjugated system at the *N*-1,3 position substituents to optimize the photophysical profiles of these BF_2 formazanate dyes for NIR-II imaging. Aniline substituents are able to form classical quinoidal structures in BF_2 formazanate, thus dramatically extending the π-system to enhance electron delocalization.[46] The different-sized nitrogen-containing rings (from aziridine to julolidine) at the *N*-1,3 position were incorporated to obtain **BF1**-**BF5** with symmetric structures. To adjust the molecular lipophilicity, the asymmetric BF_2 formazanate dyes with morpholine were also prepared at the *N1* position, and dimethylamine (**BF6**), piperidine (**BF7**), and julolidine (**BF8**) at the *N3* position.

Next, the photophysical properties of these BF_2 formazanate fluorophores were studied in organic and biological relevant mediums. The **BF1**-**BF8** dyes had NIR absorption peaks from 727 to 859 nm with large extinction coefficients of more than 44, 000 $M^{-1}cm^{-1}$ in DMSO. The dyes exhibited a red-shifting absorption trend in the order morpholine, azetidine, piperidine, pyrrolidine, and julolidine (Figure 1c). This trend was also observed in FBS (Figure S1). The fluorescence spectra for all dyes have broad emission bands ranging from 800 to 1400 nm in DMSO and FBS (Figure 1d, Figure S1). The julolidine substituent with enhanced electronic delocalization showed dramatically red-shifted absorption and fluorescence spectra, with an emission peak at 1004 nm in DMSO. TD-DFT calculations revealed strong intramolecular charge transfer (ICT) and small energy gaps (1.61– 1.74 eV) between the HOMO and LUMO, which accounted for the NIR absorption of BF_2 formazanate dyes (Figure S2, Table S1). The HOMO-LUMO energy gaps become smaller from **BF1** to **BF5** and from **BF6** to **BF8**, suggesting electron-donating groups can significantly red-shift dye absorption and emission. In toluene, tetrahydrofuran (THF), and DMSO, the dyes showed the red-shift absorption and fluorescence. In FBS, the dyes showed a hypsochromic shift absorption and decreased extinction coefficient compared to those in DMSO (Figure S3, S4). The brightness of all dyes was dramatically enhanced in solvents with lower polarity (Table S2). To assess the capabilities of BF_2 formazanate dyes for NIR-II imaging, 50 μM solutions of the dyes were imaged at different wavelengths. As shown in Figure 1e, NIR-II fluorescence properties of **BF1**-**BF8** were captured using a series of long-pass optical filters covering the NIR-II windows. To our delight, most of the dyes exhibited strong fluorescence beyond 1000 nm, with higher quantum yields comparable to other reported NIR-II fluorophores (Table S2).[8] Notably, the **BF1**-**BF8** spectra exhibited large Stokes shifts (Figure S5, S6). In particular, the **BF1** spectrum shows a 230 and 198 nm Stokes shift in DMSO and FBS that simplifies filtering of excitation light (Figure 1f). The NIR-II fluorescence behavior of all dyes was studied in deionized water (DI), phosphate-buffered saline (PBS) buffer, and FBS. The result shows all dyes have a fluorescence quench in DI and PBS. But there are relatively strong fluorescence signals over 1000 nm in FBS (Figure 1g, Figure S7). Next, the photostability of these dyes and ICG was evaluated by monitoring fluorescence intensity in DMSO and FBS. Unlike the quick degradation of the ICG, all small-molecule BF_2 formazanate dyes exhibited ultrahigh emission stabilities in the different solvents for 3 hours long-term irradiations under high laser power irradiation (808 nm, 1.5 W cm^{-2}, Figure 1h and S8a,). Photothermal and temperature-dependent

fluorescence studies showed that most dyes have appreciable photothermal conversion and significant fluorescence increase from 25 to 65 °C in FBS (Figure S8b, S8c). Figure 1i showed that dye also had high pH and chemical stability in the presence of various reactive oxygen species (ROS). Thus, BF_2 formazanate dyes can be potentially used for *in vivo* imaging in the NIR-II region.

In vitro NIR-II imaging and evaluation of BBB permeability

Before testing the use of the BF_2 formazanate dyes for *in vivo* NIR-II imaging, we first applied them for NIR-II imaging of cells in culture. U-87 MG cells were incubated in 2 μM **BF1-BF8** dyes for 20 minutes, followed by washing and imaging using an NIR-II inverted microscope.[48] Cell images showed that all dyes had good cell permeability and bright NIR-II fluorescence in cellular environment (Figure 2a). To study the subcellular localization of dyes in cell, we used commercial organelle-targeted trackers to analyze the colocalization with our dyes by confocal imaging. The result showed **BF1-BF4** and **BF6-BF8** have a better overlay with lipid-droplet, which indicates BF_2 formazanate dyes can specifically target the lipid-droplet in cells (Figure S9). Next, the cytotoxicity and photostability of these dyes were evaluated in brain vascular endothelial (bEnd.3) and U-87 MG cells, respectively. **BF1-BF8** exhibited negligible cytotoxicity even after incubation at 12 μM for 24 hours (Figure S10). We further tested the intracellular photostability of **BF1-BF8** dyes. Gratifyingly, the BF_2 formazanate dyes exhibited excellent intracellular photostability. No significant fluorescence falls of BF_2 formazanate dyes were observed during a 10 min irradiation under high laser power density (663 nm, 200 W cm^{-2}), while the intracellular fluorescence of ICG declined dramatically within 12 seconds under the same conditions (Figure 2b, 2c, and S11, supporting video 1, 2). These data confirmed that small-molecule **BF1-BF8** dyes are well-suited for *in vivo* imaging.

Physiochemical parameters, including molecular weight, lipophilicity (as calculated from log P), polar surface area, and hydrogen bonding, have been identified as key parameters for developing compounds with BBB permeability.[39–41] In general, molecules with molecular weights less than 450 Da, log P less than 5, H-bond acceptors less than 7, and H-bond donors less than 3, exhibit possible BBB permeability.[49] We calculated these parameters for BF_2 formazanate fluorophores by experimental and computational studies. For the measurement of log P, we added dyes to octanol-saturated water. The log P values were calculated based on the ratio of the dye's concentration in the water-saturated octanol phase to its concentration in the octanol-saturated aqueous phase.[50] These preliminary analyses of **BF1-BF8** indicated that BF_2 formazanate dyes exhibited attractive physicochemical parameters for the potential BBB permeability (Table S3). To further evaluate the BBB permeability of BF_2 formazanate dyes, we used an *in vitro* BBB model prepared by seeding bEnd.3 cells onto gelatin-coated upper chambers of the transwell plates (Figure 2d). Successful establishment of the BBB layer was confirmed by the stable transendothelial electrical resistance (TEER) value (Figure S12). BF_2 formazanate dyes (**BF1-BF8**, 5 μM) were then added to the upper chambers, and dye absorbance values in the lower chambers were measured at different time points (30, 60, 90, 120 min). Evans Blue (EB), which is incapable of passing through the BBB, was used as the negative control.[51,52] By calculating the transcellular diffusion efficiency based on standard curves of Figure S13, **BF1** and **BF6**

exhibited significantly higher BBB permeabilities among the BF_2 formazanate dyes tested, reaching an appreciable concentration in the lower chambers within 2 hours. In contrast, the slow absorbance increased in lower chambers for **BF2**-**BF5**, **BF7**, **BF8**, and EB, indicating a low rate of BBB penetration for these dyes (Figure 2e). To study the imaging performance of dyes, **BF1** and **BF6** were chosen to investigate the scattering and penetration in mimic tissue. Even up to 5 millimeters mimic tissue depth, the fluorescence signals of two dyes were clearly observed (Figure 2f–i).

In vivo brain imaging using NIR-II fluorescence

Encouraged by the NIR-II imaging properties and promising physicochemical parameters of BF_2 formazanate dyes and their ability to cross *in vitro* BBB monolayers, we explored the ability of these dyes to cross the BBB *in vivo.* To evaluate the use of the dyes for NIR-II imaging of cerebral tissue, we used tail vein injections to introduce **BF1-BF8** dyes into athymic nude mice, followed by *in vivo* NIR-II fluorescence imaging. ICG, a dye that has previously been used for *in vivo* NIR-II fluorescence imaging cerebrovascular, was included for comparison.[53] As shown in Figure 3a and 3c, significant **BF1** and **BF6** fluorescence signals were observed in brain tissue after injection. The NIR-II fluorescence intensities of **BF1** and **BF6** reached maximum values 20 and 45 minutes after injection, respectively. In contrast to the blurred images obtained with visible and NIR-I light, sharp cerebral images with high signal-to-noise ratios (SNR) of 2.5–2.9 were obtained for the **BF1** and **BF6** dyes (Figure 3b, 3d). In contrast, no significant NIR-II signals in cerebral tissue were observed after the injection of **BF2**, **BF3**, **BF4**, **BF5**, **BF7**, or **BF8** (Figure S14). As shown in Figure 3e and 3f, ICG-treated mice exhibited fluorescence signals only in major brain blood vessels, rather than in the brain parenchyma. This vessel fluorescence gradually decreased after administration, and no fluorescence was observed from the brain tissue itself. This result is consistent with previous reports that ICG cannot penetrate the BBB.[30,53] At 2 hours post-injection, multiple organs, including brain, heart, lung, kidney, spleen, liver, intestine, stomach, bone, muscle, and pancreas, were isolated and used for *ex vivo* NIR-II imaging. *Ex vivo* fluorescence images indicated that significant amounts of **BF1** and **BF6** accumulated in brain tissue (Figure 3g and 3h). The biodistribution of **BF1** and **BF6** after 14 hours revealed that liver, kidneys, and bladder were successively illuminated (Figure S15). To further confirm BBB permeability of the **BF1** and **BF6**, brain homogenates from mice injected with these dyes were subjected to mass spectrometry analysis. Single ion monitoring (SIM) mass spectrometry revealed peaks of [m/z + H] = 468.2 and 426.2, corresponding to the molecular weights of **BF1** and **BF6** (Figure 3i and 3j). High-performance liquid chromatography (HPLC) analysis showed that **BF1** and **BF6** have accumulated in the brain tissue after injection compared to the standard curves (Figure 3k). This confirmed the high BBB permeability of **BF1** and **BF6**. **BF6** was chosen for further study due to its higher SNR.

We next studied the process of dye diffusion through the BBB. Prior to imaging, the mouse scalp was surgically opened under anesthesia to avoid interference from scalp vessels. Within the first 90s post injection, **BF6** brightly illuminated brain vessels more obvious than brain tissues upon excitation with the 808 nm laser (Figure 3l). And with the diffusion of **BF6** from intracranial vessels to brain tissues, the entire brain was illuminated so

that no clear boundary was seen between the blood vessels and brain tissues (supporting video3). Quantitative fluorescence data indicated that the NIR-II fluorescence ratio between tissue and vessels gradually increased within 160 s (Figure 3m and 3n). The fluorescence intensity of brain tissue overtook that of intracranial vessels in 100 s, suggesting rapid BBB permeability of the **BF6** in vivo. **BF1**-treated mice exhibited a similarly rapid diffusion of the dye from vessels into brain tissue (Figure S16). By comparison, the mice treated with ICG, the NIR-II signal was restricted to blood vessels and additional diffusion into the brain tissue was not observed over time (Figure 3l, 3o, and 3p), which means the ICG dye is unable to cross the BBB. Based on the NIR-II fluorescent images of ICG, we found the diameter of brain vessels to be about 508 μm, and it was consistent during the whole imaging process. While for the imaging with **BF6**, the calculated diameter of the intracranial vessels was about 663 μm, which was larger than that of ICG because of BBB diffusion of **BF6** (Figure S17).

Importantly, no overt signs of toxicity were observed in mice treated with multi-doses **BF1** and **BF6** dyes. One month after the dye injection, mice were euthanized for collection of major organs, including heart, liver, spleen, lung, kidneys, and brain. Hematoxylin and eosin (H&E) staining of tissue sections suggested that **BF1** and **BF6** exhibited negligible toxicity in major organs compared with PBS-treated mice (Figure S18).

Biodistribution of BF_2 Formazanate Dyes in a Mouse Model of Glioblastoma

Glioblastoma multiforme is a uniformly fatal brain tumor characterized by infiltrative growth supported by angiogenesis. Glioblastoma-associated blood vessels are markedly abnormal, resulting in edema, hypoxia, and decreased delivery of chemotherapeutic agents.[54] Hoping that formazanate-based reagents might represent a novel approach to imaging glioblastoma, we explored the biodistribution of **BF1** and **BF6** in mice with GBM models. We introduced murine U87-MG GBM cells into the brain of nude mice based on a previously reported protocol.[55,56] 3–4 weeks after tumor implantation, we injected ICG solution intravenously into the mice, followed by noninvasive imaging of the intact brains using NIR-II fluorescence. After 24 hours, **BF1** or **BF6** was used to treat the same mice with ICG treatment, followed by the noninvasive imaging again. Due to the fast metabolism of ICG in living mice, we collected fluorescent brain images at a six-time points within 120 seconds, while the images of **BF1** and **BF6**-treated mice were collected within 60 minutes. As shown in Figure 4a and 4b, irregular brain vessels were clearly illuminated by ICG, which indicates the glioma existence in the mouse brains. During 120 seconds, the fluorescence signals of ICG always were restricted in the vessels and gradually disappeared. It confirmed that BBB prevents ICG from leaking into brain tissues in the presence of glioma. Surprisingly, we found the brains bearing tumors showed uneven fluorescence imaging, and fluorescence intensity of partial brain tissues increased from 0 to 60 minutes after **BF1** and **BF6** injection (Figure 4a and 4b). The cross-section fluorescence intensity profiles showed a significant difference between the ICG and **BF1** or **BF6** implying their different imaging behaviors (Figure 4c, 4d). Following *in vivo* imaging, mice were euthanized and brain tissues were collected for *ex vivo* studies. *Ex vivo* imaging showed a similar result with the *in vivo* imaging (Figure S19a, S19b). After the *ex vivo* imaging, brains were sliced and stained using Congo red and H&E for a detailed study. Isolated

brains were characterized by obvious pathological features such as glioma-related edema (yellow arrows, Figure S19c, S19d) from three tangents along white dash lines in brain tissues. Most importantly, these results demonstrated that normal and brain tumor tissues were easily differentiated and delineated the margins using *in vivo* and *ex vivo* NIR-II fluorescence imaging. Time-dependent normal-to-glioma ratio (NGR) changes determined by the NIR-II fluorescence imaging of brain normal tissue and glioma after ICG, **BF1**, or **BF6** treatment (Figure S20a, S20b, S20d, S20e). Compared with ICG, brain images of **BF1**- and **BF6**-treated mice established a significantly larger NGR, suggesting **BF1** and **BF6** can better differentiate normal tissue from glioma than ICG (Figure S20c, S20f). Interestingly, we found that **BF1**- or **BF6**-treated mice exhibited higher fluorescence in normal tissue than in malignant tissue. To exclude the possibility that fluorescence differences were induced by the tumor microenvironment, the effect of pH and ROS stabilities on **BF1** and **BF6** fluorescence was tested. Like **BF1**, under low pH and oxidative environment, **BF6** showed only minor changes in fluorescence (Figure S21 and S22). Another possible reason for the observed fluorescent differences in normal and malignant tissues may be the fluid pressure. Recent studies suggested that there is an increasing interstitial and intracranial fluid pressure in glioma regions, which may limit the diffusion of the dyes from blood vessels.[57–59] The other potential reason can be the lack of transcellular and efflux transporters in the glioma niche. Overall, these results indicated that BF_2 formazanate dyes were potential tools for differentiating GBM tissue during different growth times, thus facilitating image-guided intervention in the clinic.

CONCLUSIONS

In summary, our work developed a series of NIR-II fluorophores that had ultrahigh photostability, high biological stability, large Stokes shift, relatively strong brightness, and capability to cross the BBB. Compared to other recently reported “small-molecule” NIR-II fluorophore scaffolds, BF_2 formazanate NIR-II dyes have key physicochemical parameters for the potential BBB permeability. We found that BF_2 formazanate fluorophores modified with morpholine can efficiently penetrate the BBB, which allows NIR-II brain imaging *in vivo* through the intact skin and skull. In a murine glioblastoma model, BF_2 formazanate fluorescence can be used to distinguish between tumor and normal tissue. Our work thus generates a new class of NIR-II fluorophores that are small in size and exhibit ideal lipophilicity, low polar surface areas, and adjustable photophysical properties, which provides a promising structural scaffold for the design of brain imaging and therapeutic probes.

Supplementary Material

Refer to Web version on PubMed Central for supplementary material.

ACKNOWLEDGMENTS

This work was supported by the Cancer Prevention Research Institute of Texas (CPRIT, RR170014 to H.X.), NIH (R35-GM133706 to H.X., R21-CA255894 to H.X.), U.S. Department of Defense (W81XWH-21-1-0789 to H.X.), the Robert A. Welch Foundation (C-1970 to H.X. and C-0807 to R.B.W.), the National Science Foundation (CHE-1803066 and CHE-2203309 to R.B.W.), the Hamill Innovation Award (Hamill Foundation), the John S. Dunn Foundation Collaborative Research Award (Gulf Coast Consortia), and the Department of Radiology,

Stanford University (Z.C.). H. X. is a Cancer Prevention & Research Institute of Texas (CPRIT) Scholar in Cancer Research. We are grateful to V.B. Espinoza for experimental assistance.

REFERENCES

(1). Li C; Cao L; Zhang Y; Yi P; Wang M; Tan B; Deng Z; Wu D; Wang Q Preoperative Detection and Intraoperative Visualization of Brain Tumors for More Precise Surgery: A New Dual-Modality MRI and NIR Nanoprobe. Small Weinh. Bergstr. Ger. 2015, 11 (35), 4517–4525. 10.1002/smll.201500997.

(2). Sim C; Kim H; Moon H; Lee H; Chang JH; Kim H Photoacoustic-Based Nanomedicine for Cancer Diagnosis and Therapy. J. Control. Release Off. J. Control. Release Soc. 2015, 203, 118–125. 10.1016/j.jconrel.2015.02.020.

(3). Adams S; Baum RP; Stuckensen T; Bitter K; Hör G Prospective Comparison of 18F-FDG PET with Conventional Imaging Modalities (CT, MRI, US) in Lymph Node Staging of Head and Neck Cancer. Eur. J. Nucl. Med. 1998, 25 (9), 1255–1260. 10.1007/s002590050293. [PubMed: 9724374]

(4). Sheng Z; Guo B; Hu D; Xu S; Wu W; Liew WH; Yao K; Jiang J; Liu C; Zheng H; Liu B Bright Aggregation-Induced-Emission Dots for Targeted Synergetic NIR-II Fluorescence and NIR-I Photoacoustic Imaging of Orthotopic Brain Tumors. Adv. Mater. Deerfield Beach Fla 2018, e1800766. 10.1002/adma.201800766.

(5). Kircher MF; de la Zerda A; Jokerst JV; Zavaleta CL; Kempen PJ; Mittra E; Pitter K; Huang R; Campos C; Habte F; Sinclair R; Brennan CW; Mellinghoff IK; Holland EC; Gambhir SS A Brain Tumor Molecular Imaging Strategy Using a New Triple-Modality MRI-Photoacoustic-Raman Nanoparticle. Nat. Med. 2012, 18 (5), 829–834. 10.1038/nm.2721. [PubMed: 22504484]

(6). Kim MM; Parolia A; Dunphy MP; Venneti S Non-Invasive Metabolic Imaging of Brain Tumours in the Era of Precision Medicine. Nat. Rev. Clin. Oncol. 2016, 13 (12), 725–739. 10.1038/nrclinonc.2016.108. [PubMed: 27430748]

(7). Li C; Chen G; Zhang Y; Wu F; Wang Q Advanced Fluorescence Imaging Technology in the Near-Infrared-II Window for Biomedical Applications. J Am Chem Soc 2020, 142 (35), 14789–14804. 10.1021/jacs.0c07022. [PubMed: 32786771]

(8). Lei Z; Zhang F Molecular Engineering of NIR-II Fluorophores for Improved Biomedical Detection. Angew. Chem. 2021, 133 (30), 16430–16444. 10.1002/ange.202007040.

(9). Dai H; Shen Q; Shao J; Wang W; Gao F; Dong X Small Molecular NIR-II Fluorophores for Cancer Phototheranostics. The Innovation 2021, 2 (1), 100082. 10.1016/j.xinn.2021.100082. [PubMed: 34557737]

(10). Hong G; Antaris AL; Dai H Near-Infrared Fluorophores for Biomedical Imaging. Nat. Biomed. Eng. 2017, 1 (1), 1–22. 10.1038/s41551-016-0010.

(11). Mu J; Xiao M; Shi Y; Geng X; Li H; Yin Y; Chen X The Chemistry of Organic Contrast Agents in the NIR-II Window. Angew. Chem. Int. Ed. 2021, anie.202114722. 10.1002/anie.202114722.

(12). Thimsen E; Sadtler B; Berezin MY Shortwave-Infrared (SWIR) Emitters for Biological Imaging: A Review of Challenges and Opportunities. Nanophotonics 2017, 6 (5), 1043–1054. 10.1515/nanoph-2017-0039.

(13). Huang J; Pu K Activatable Molecular Probes for Second Near-Infrared Fluorescence, Chemiluminescence, and Photoacoustic Imaging. Angew. Chem. Int. Ed. 2020, 59 (29), 11717–11731. 10.1002/anie.202001783.

(14). Hong G; Lee JC; Robinson JT; Raaz U; Xie L; Huang NF; Cooke JP; Dai H Multifunctional in Vivo Vascular Imaging Using Near-Infrared II Fluorescence. Nat. Med. 2012, 18 (12), 1841–1846. 10.1038/nm.2995. [PubMed: 23160236]

(15). Cao J; Zhu B; Zheng K; He S; Meng L; Song J; Yang H Recent Progress in NIR-II Contrast Agent for Biological Imaging. Front. Bioeng. Biotechnol. 2020, 7, 487. 10.3389/fbioe.2019.00487. [PubMed: 32083067]

(16). Hu Z; Fang C; Li B; Zhang Z; Cao C; Cai M; Su S; Sun X; Shi X; Li C; Zhou T; Zhang Y; Chi C; He P; Xia X; Chen Y; Gambhir SS; Cheng Z; Tian J First-in-Human Liver-Tumour Surgery Guided by Multispectral Fluorescence Imaging in the Visible and near-Infrared-I/II Windows. Nat. Biomed. Eng. 2020, 4 (3), 259–271. 10.1038/s41551-019-0494-0. [PubMed: 31873212]

(17). Carr JA; Valdez TA; Bruns OT; Bawendi MG Using the Shortwave Infrared to Image Middle Ear Pathologies. Proc. Natl. Acad. Sci. U. S. A. 2016, 113 (36), 9989–9994. 10.1073/pnas.1610529113. [PubMed: 27551085]

(18). Zhong Y; Ma Z; Wang F; Wang X; Yang Y; Liu Y; Zhao X; Li J; Du H; Zhang M; Cui Q; Zhu S; Sun Q; Wan H; Tian Y; Liu Q; Wang W; Garcia KC; Dai H In Vivo Molecular Imaging for Immunotherapy Using Ultra-Bright near-Infrared-IIb Rare-Earth Nanoparticles. Nat. Biotechnol. 2019, 37 (11), 1322–1331. 10.1038/s41587-019-0262-4. [PubMed: 31570897]

(19). Naczynski DJ; Tan MC; Zevon M; Wall B; Kohl J; Kulesa A; Chen S; Roth CM; Riman RE; Moghe PV Rare-Earth-Doped Biological Composites as in Vivo Shortwave Infrared Reporters. Nat. Commun. 2013, 4, 2199. 10.1038/ncomms3199. [PubMed: 23873342]

(20). Bruns OT; Bischof TS; Harris DK; Franke D; Shi Y; Riedemann L; Bartelt A; Jaworski FB; Carr JA; Rowlands CJ; Wilson MWB; Chen O; Wei H; Hwang GW; Montana DM; Coropceanu I; Achorn OB; Kloepper J; Heeren J; So PTC; Fukumura D; Jensen KF; Jain RK; Bawendi MG Next-Generation in Vivo Optical Imaging with Short-Wave Infrared Quantum Dots. Nat. Biomed. Eng. 2017, 1. 10.1038/s41551-017-0056.

(21). Hong G; Robinson JT; Zhang Y; Diao S; Antaris AL; Wang Q; Dai H In Vivo Fluorescence Imaging with Ag2S Quantum Dots in the Second Near-Infrared Region. Angew. Chem. Int. Ed Engl. 2012, 51 (39), 9818–9821. 10.1002/anie.201206059. [PubMed: 22951900]

(22). Ceppi L; Bardhan NM; Na Y; Siegel A; Rajan N; Fruscio R; Del Carmen MG; Belcher AM; Birrer MJ Real-Time Single-Walled Carbon Nanotube-Based Fluorescence Imaging Improves Survival after Debulking Surgery in an Ovarian Cancer Model. ACS Nano 2019, 13 (5), 5356–5365. 10.1021/acsnano.8b09829. [PubMed: 31009198]

(23). Chang B; Li D; Ren Y; Qu C; Shi X; Liu R; Liu H; Tian J; Hu Z; Sun T; Cheng Z A Phosphorescent Probe for in Vivo Imaging in the Second Near-Infrared Window. Nat. Biomed. Eng. 2021. 10.1038/s41551-021-00773-2.

(24). Chen H; Shou K; Chen S; Qu C; Wang Z; Jiang L; Zhu M; Ding B; Qian K; Ji A; Lou H; Tong L; Hsu A; Wang Y; Felsher DW; Hu Z; Tian J; Cheng Z Smart Self-Assembly Amphiphilic Cyclopeptide-Dye for Near-Infrared Window-II Imaging. Adv. Mater. 2021, 33 (16), 2006902. 10.1002/adma.202006902.

(25). Yang Q; Ma Z; Wang H; Zhou B; Zhu S; Zhong Y; Wang J; Wan H; Antaris A; Ma R; Zhang X; Yang J; Zhang X; Sun H; Liu W; Liang Y; Dai H Rational Design of Molecular Fluorophores for Biological Imaging in the NIR-II Window. Adv. Mater. Deerfield Beach Fla 2017, 29 (12). 10.1002/adma.201605497.

(26). Liu D; He Z; Zhao Y; Yang Y; Shi W; Li X; Ma H Xanthene-Based NIR-II Dyes for In Vivo Dynamic Imaging of Blood Circulation. J. Am. Chem. Soc. 2021, jacs.1c07711. 10.1021/jacs.1c07711.

(27). Li B; Lu L; Zhao M; Lei Z; Zhang F An Efficient 1064 Nm NIR-II Excitation Fluorescent Molecular Dye for Deep-Tissue High-Resolution Dynamic Bioimaging. Angew. Chem. 2018, 130 (25), 7605–7609. 10.1002/ange.201801226.

(28). Bai L; Sun P; Liu Y; Zhang H; Hu W; Zhang W; Liu Z; Fan Q; Li L; Huang W Novel Aza-BODIPY Based Small Molecular NIR-II Fluorophores for *in Vivo* Imaging. Chem. Commun. 2019, 55 (73), 10920–10923. 10.1039/C9CC03378E.

(29). Li L; Dong X; Li J; Wei J A Short Review on NIR-II Organic Small Molecule Dyes. Dyes Pigments 2020, 183, 108756. 10.1016/j.dyepig.2020.108756.

(30). Cai Z; Zhu L; Wang M; Roe AW; Xi W; Qian J NIR-II Fluorescence Microscopic Imaging of Cortical Vasculature in Non-Human Primates. Theranostics 2020, 10 (9), 4265–4276. 10.7150/thno.43533. [PubMed: 32226552]

(31). Starosolski Z; Bhavane R; Ghaghada KB; Vasudevan SA; Kaay A; Annapragada A Indocyanine Green Fluorescence in Second Near-Infrared (NIR-II) Window. PloS One 2017, 12 (11), e0187563. 10.1371/journal.pone.0187563. [PubMed: 29121078]

(32). Carr JA; Franke D; Caram JR; Perkinson CF; Saif M; Askoxylakis V; Datta M; Fukumura D; Jain RK; Bawendi MG; Bruns OT Shortwave Infrared Fluorescence Imaging with the Clinically Approved Near-Infrared Dye Indocyanine Green. Proc. Natl. Acad. Sci. 2018, 115 (17), 4465–4470. 10.1073/pnas.1718917115. [PubMed: 29626132]

(33). Antaris AL; Chen H; Diao S; Ma Z; Zhang Z; Zhu S; Wang J; Lozano AX; Fan Q; Chew L; Zhu M; Cheng K; Hong X; Dai H; Cheng Z A High Quantum Yield Molecule-Protein Complex Fluorophore for near-Infrared II Imaging. Nat Commun 2017, 8 (1), 15269. 10.1038/ncomms15269. [PubMed: 28524850]

(34). Zhu S; Hu Z; Tian R; Yung BC; Yang Q; Zhao S; Kiesewetter DO; Niu G; Sun H; Antaris AL; Chen X Repurposing Cyanine NIR-I Dyes Accelerates Clinical Translation of Near-Infrared-II (NIR-II) Bioimaging. Adv Mater 2018, 30 (34), e1802546. 10.1002/adma.201802546.

(35). Cosco ED; Spearman AL; Ramakrishnan S; Lingg JGP; Saccomano M; Pengshung M; Arús BA; Wong KCY; Glasl S; Ntziachristos V; Warmer M; McLaughlin RR; Bruns OT; Sletten EM Shortwave Infrared Polymethine Fluorophores Matched to Excitation Lasers Enable Non-Invasive, Multicolour in Vivo Imaging in Real Time. Nat. Chem. 2020, 12 (12), 1123–1130. 10.1038/s41557-020-00554-5. [PubMed: 33077925]

(36). Antaris AL; Chen H; Cheng K; Sun Y; Hong G; Qu C; Diao S; Deng Z; Hu X; Zhang B; Zhang X; Yaghi OK; Alamparambil ZR; Hong X; Cheng Z; Dai H A Small-Molecule Dye for NIR-II Imaging. Nat. Mater. 2016, 15 (2), 235–242. 10.1038/nmat4476. [PubMed: 26595119]

(37). Cosco ED; Caram JR; Bruns OT; Franke D; Day RA; Farr EP; Bawendi MG; Sletten EM Flavylium Polymethine Fluorophores for Near- and Shortwave Infrared Imaging. Angew. Chem. Int. Ed Engl. 2017, 56 (42), 13126–13129. 10.1002/anie.201706974. [PubMed: 28806473]

(38). Lipinski CA; Lombardo F; Dominy BW; Feeney PJ Experimental and Computational Approaches to Estimate Solubility and Permeability in Drug Discovery and Development Settings. Adv. Drug Deliv. Rev. 2001, 46 (1–3), 3–26. 10.1016/s0169-409x(00)00129-0. [PubMed: 11259830]

(39). Mikitsh JL; Chacko A-M Pathways for Small Molecule Delivery to the Central Nervous System across the Blood-Brain Barrier. Perspect. Med. Chem. 2014, 6, 11–24. 10.4137/PMC.S13384.

(40). Habgood MD; Begley DJ; Abbott NJ Determinants of Passive Drug Entry into the Central Nervous System. Cell. Mol. Neurobiol. 2000, 20 (2), 231–253. 10.1023/a:1007001923498. [PubMed: 10696512]

(41). Pardridge WM Drug Transport across the Blood-Brain Barrier. J. Cereb. Blood Flow Metab. Off. J. Int. Soc. Cereb. Blood Flow Metab. 2012, 32 (11), 1959–1972. 10.1038/jcbfm.2012.126.

(42). Gilroy JB; Otten E Formazanate Coordination Compounds: Synthesis, Reactivity, and Applications. Chem. Soc. Rev. 2020, 49 (1), 85–113. 10.1039/c9cs00676a. [PubMed: 31802081]

(43). Barbon SM; Price JT; Reinkeluers PA; Gilroy JB Substituent-Dependent Optical and Electrochemical Properties of Triarylformazanate Boron Difluoride Complexes. Inorg. Chem. 2014, 53 (19), 10585–10593. 10.1021/ic5016912. [PubMed: 25226240]

(44). Maar RR; Barbon SM; Sharma N; Groom H; Luyt LG; Gilroy JB Evaluation of Anisole-Substituted Boron Difluoride Formazanate Complexes for Fluorescence Cell Imaging. Chem. – Eur. J. 2015, 21 (44), 15589–15599. 10.1002/chem.201502821. [PubMed: 26397738]

(45). Chang M-C; Chantzis A; Jacquemin D; Otten E Boron Difluorides with Formazanate Ligands: Redox-Switchable Fluorescent Dyes with Large Stokes Shifts. Dalton Trans. Camb. Engl. 2003 2016, 45 (23), 9477–9484. 10.1039/c6dt01226d.

(46). Maar RR; Zhang R; Stephens DG; Ding Z; Gilroy JB Near-Infrared Photoluminescence and Electrochemiluminescence from a Remarkably Simple Boron Difluoride Formazanate Dye. Angew. Chem. Int. Ed. 2019, 58 (4), 1052–1056. 10.1002/anie.201811144.

(47). Buguis FL; Maar RR; Staroverov VN; Gilroy JB Near-Infrared Boron Difluoride Formazanate Dyes. Chem. – Eur. J. 2021, 27 (8), 2854–2860. 10.1002/chem.202004793. [PubMed: 33140465]

(48). Cherukuri P; Bachilo SM; Litovsky SH; Weisman RB Near-Infrared Fluorescence Microscopy of Single-Walled Carbon Nanotubes in Phagocytic Cells. J. Am. Chem. Soc. 2004, 126 (48), 15638–15639. 10.1021/ja0466311. [PubMed: 15571374]

(49). Pajouhesh H; Lenz GR Medicinal Chemical Properties of Successful Central Nervous System Drugs. NeuroRX 2005, 2 (4), 541–553. 10.1602/neurorx.2.4.541. [PubMed: 16489364]

(50). Ran C; Xu X; Raymond SB; Ferrara BJ; Neal K; Bacskai BJ; Medarova Z; Moore A Design, Synthesis, and Testing of Difluoroboron-Derivatized Curcumins as Near-Infrared Probes for in Vivo Detection of Amyloid-β Deposits. J. Am. Chem. Soc. 2009, 131 (42), 15257–15261. 10.1021/ja9047043. [PubMed: 19807070]

(51). Wang S; Sheng Z; Yang Z; Hu D; Long X; Feng G; Liu Y; Yuan Z; Zhang J; Zheng H; Zhang X Activatable Small-Molecule Photoacoustic Probes That Cross the Blood-Brain Barrier for Visualization of Copper(II) in Mice with Alzheimer's Disease. Angew Chem Int Ed Engl 2019, 58 (36), 12415–12419. 10.1002/anie.201904047. [PubMed: 31309679]

(52). Kim Y-A; Park SL; Kim M-Y; Lee SH; Baik EJ; Moon C-H; Jung Y-S Role of PKCβII and PKCδ in Blood–Brain Barrier Permeability during Aglycemic Hypoxia. Neurosci. Lett. 2010, 468 (3), 254–258. 10.1016/j.neulet.2009.11.007. [PubMed: 19900507]

(53). Bhavane R; Starosolski Z; Stupin I; Ghaghada KB; Annapragada A NIR-II Fluorescence Imaging Using Indocyanine Green Nanoparticles. Sci. Rep. 2018, 8 (1), 14455. 10.1038/s41598-018-32754-y. [PubMed: 30262808]

(54). Tate MC; Aghi MK Biology of Angiogenesis and Invasion in Glioma. Neurotherapeutics 2009, 6 (3), 447–457. 10.1016/j.nurt.2009.04.001. [PubMed: 19560735]

(55). Kurbegovic S; Juhl K; Chen H; Qu C; Ding B; Leth JM; Drzewiecki KT; Kjaer A; Cheng Z Molecular Targeted NIR-II Probe for Image-Guided Brain Tumor Surgery. Bioconjug. Chem. 2018, 29 (11), 3833–3840. 10.1021/acs.bioconjchem.8b00669. [PubMed: 30296054]

(56). Xiao F; Lin L; Chao Z; Shao C; Chen Z; Wei Z; Lu J; Huang Y; Li L; Liu Q; Liang Y; Tian L Organic Spherical Nucleic Acids for the Transport of a NIR-II-Emitting Dye Across the Blood–Brain Barrier. Angew. Chem. Int. Ed. 2020, 59 (24), 9702–9710. 10.1002/anie.202002312.

(57). Arvanitis CD; Ferraro GB; Jain RK The Blood–Brain Barrier and Blood–Tumour Barrier in Brain Tumours and Metastases. Nat. Rev. Cancer 2020, 20 (1), 26–41. 10.1038/s41568-019-0205-x. [PubMed: 31601988]

(58). Rosińska S; Gavard J Tumor Vessels Fuel the Fire in Glioblastoma. Int. J. Mol. Sci. 2021, 22 (12), 6514. 10.3390/ijms002D6514. [PubMed: 34204510]

(59). Haumann R; Videira JC; Kaspers GJL; van Vuurden DG; Hulleman E Overview of Current Drug Delivery Methods Across the Blood–Brain Barrier for the Treatment of Primary Brain Tumors. CNS Drugs 2020, 34 (11), 1121–1131. 10.1007/s40263-020-00766-w. [PubMed: 32965590]

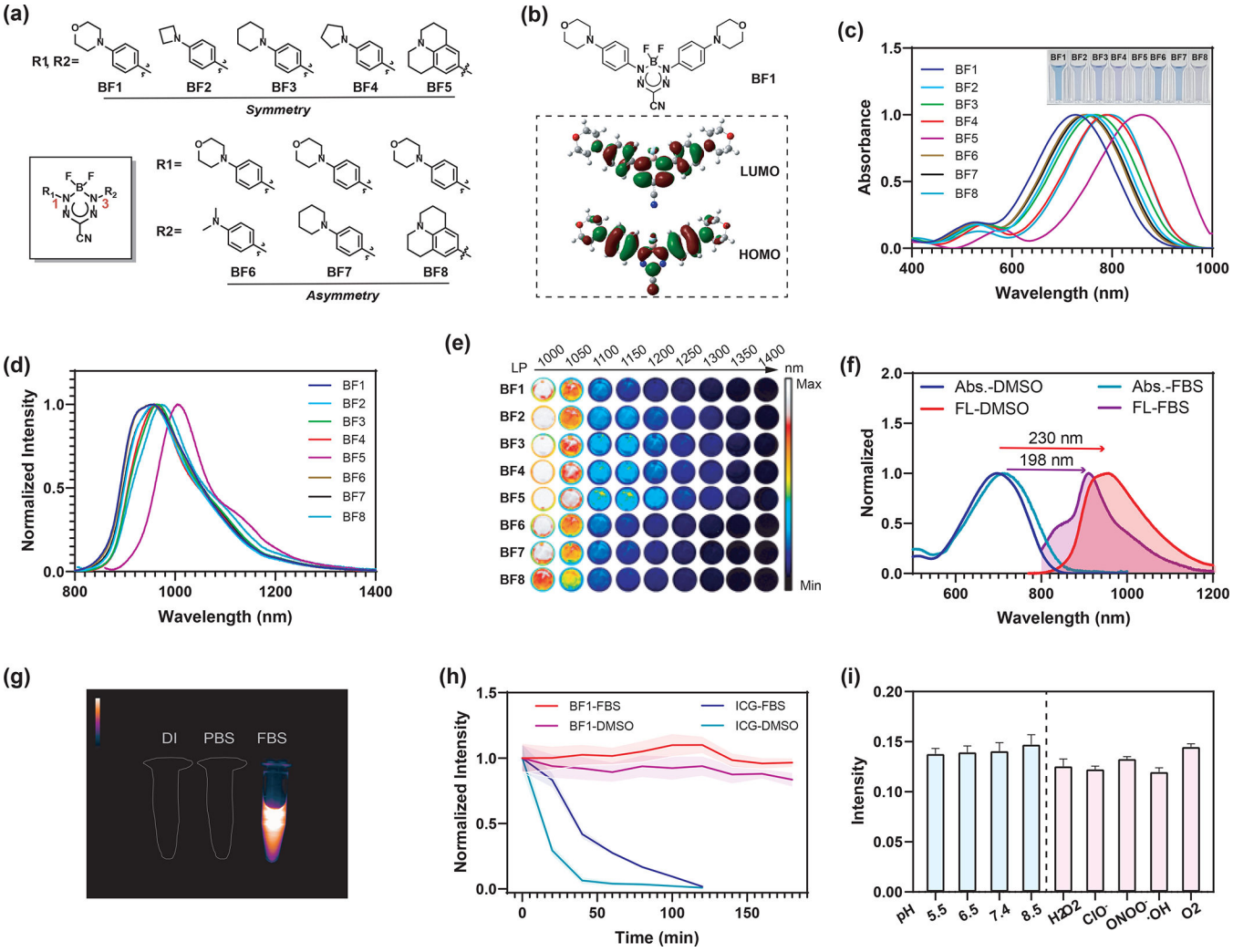

Figure 1.

(a) Structures of BF_2 formazanate dyes **BF1-BF8** in this study. **(b)** HOMOs and LUMOs calculated for **BF1**. **(c)** The normalized absorbance spectra of **BF1-BF8** (20 μM) solution in DMSO. Inset shows photos of the solutions. **(d)** The normalized fluorescence spectra of **BF1-BF8** (20 μM) in DMSO. **(e)** False-colored images of **BF1-BF8** at 50 μM collected through long-pass (LP) filters with cut-on wavelengths of 1000, 1050, 1100, 1150, 1200, 1250, 1300, 1350, and 1400 nm illumination was at 808 nm laser (45 mW cm^{-2}, 250 ms exposure). (**f**) Stokes shift of **BF1** with a concentration of 10 μM in DMSO and FBS. **(g)** NIR-II fluorescence images of **BF1** (10 μM) in deionized water (DI), PBS buffer, and FBS. (**h**) Stability of **BF1** and **ICG** (10 μM) under 808 nm light radiation within 180 minutes in FBS and DMSO. (**i**) Fluorescent stability of **BF1** (10 μM) in PBS (1% FBS) buffer with different pH and ROS species.

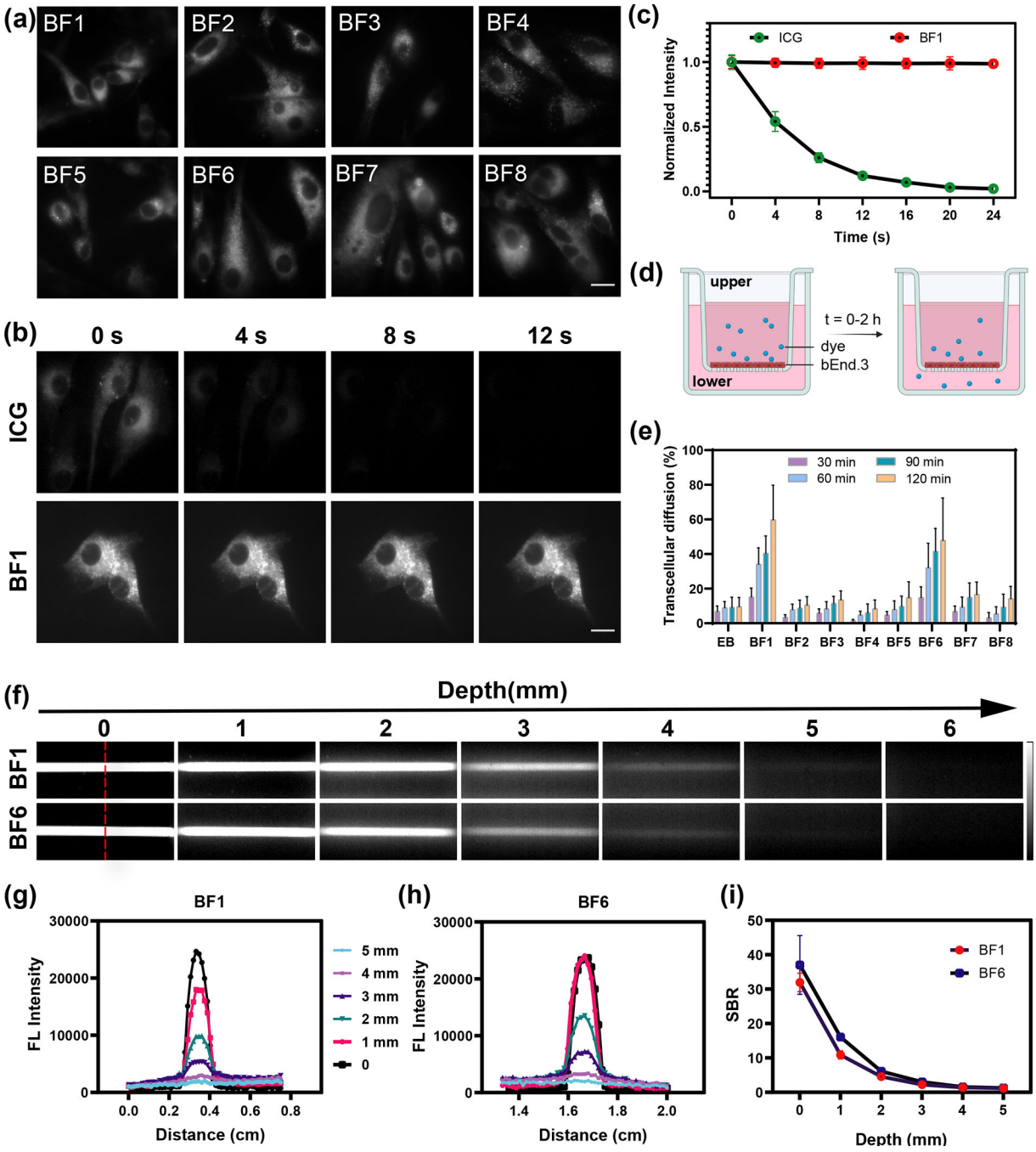

Figure 2.

(a) Fluorescence imaging of **BF1- BF8** in U-87 MG cells. All cell imaging experiments were performed using an NIR-II microscope with a 663 nm excitation laser (200 W cm^{-2}, exposure 10 ms) and 950 ± 50 nm emission filter. Scale bar is 10 μm. **(b)** Fluorescence imaging of ICG and **BF1** in U-87 MG cells at 0, 4, 8, 12 s under laser irradiation. Scale bar is 10 μm. **(c)** Cellular photostability curves of **ICG** and **BF1** within 25 seconds. **(d)** Schematic diagram of *in vitro* BBB model used in this study. **(e)** The relative transcellular diffusion amount of **BF1-BF8** and **EB** *in vitro* within 2 hours. **(f)** Fluorescence images

(excitation 808 nm, LP 1000 nm) of the capillary tube filled with **BF1** and **BF6** at depths of 0–6 mm in 1% Intralipid mimic tissue. **(g, h)** The cross-sectional fluorescence intensity profiles of **BF1** and **BF6** along the red dash line in (f) at different tissue depths. **(i)** The signal-background ratio (SBR) curves of **BF1** and **BF6** in 1% Intralipid®.

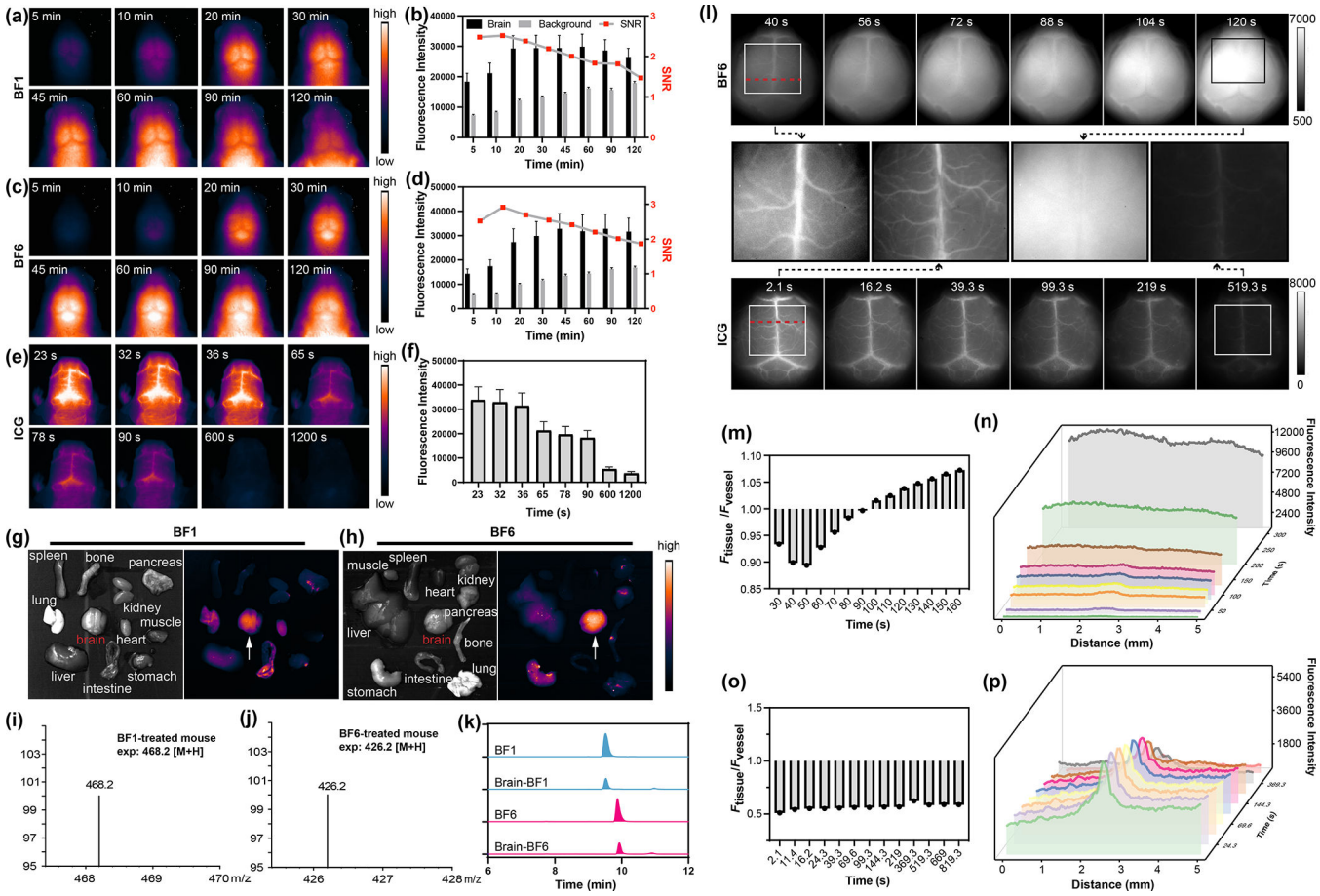

Figure 3.

(a) *In vivo* NIR-II fluorescence imaging of cerebral tissue of mice injected with **BF1** (200 μL, 200 μM, tail vein injection) at time intervals from 5 to 120 min. (70 mW cm^{-2}, 808 nm laser, 1000 nm LP filter). **(b)** Time-dependent signal-to-noise ratio (SNR) changes determined by the NIR-II fluorescence imaging of **BF1**-treated mice. **(c)** *In vivo* NIR-II fluorescence imaging of cerebral tissue of mice injected with **BF6** as described in (a). **(d)** SNR changes of **BF6**-treated mice. **(e)** *In vivo* NIR-II fluorescence imaging of cerebral tissue from nude mice injected with ICG (200 μL, 200 μM) at certain time intervals from 5 s to 1200 s. **(f)** The fluorescence intensity changes of the brain at designated time points. **(g, h)** The fluorescence images of the heart, lung, kidney, spleen, liver, brain, intestine, stomach, bone, muscle, and pancreas at 2 hour after the injection of **BF1** and **BF6**. **(i, j)** Mass spectra from extracted brain tissue of mice after intravenous injection of **BF1** and **BF6** for 1 hour. (**k**) HPLC spectra of **BF1**, **BF6** standards and responding brain homogenate of mice treated with **BF1** and **BF6**. **(l)** *In vivo* NIR-II fluorescence imaging change of brain vessels and tissue at different time points after intravenous injection of **BF6** and ICG. **(m)** Fluorescence ratio changes of brain tissue and vessel after intravenous injection of **BF6** in (**l**) at different time points. **(n)** Cross sectional fluorescence intensity profile along the red dash line in (**l**) collected by a 1000 nm long-pass filter at designated time points after intravenous injection of **BF6**. **(o)** Fluorescence ratio changes of brain tissue and vessel after intravenous injection of ICG in (**l**) at different time points. **(p)** Cross sectional fluorescence intensity profile along

the red line in (**l**) collected by a 1000 nm long-pass filter at designated time points after intravenous injection of ICG.

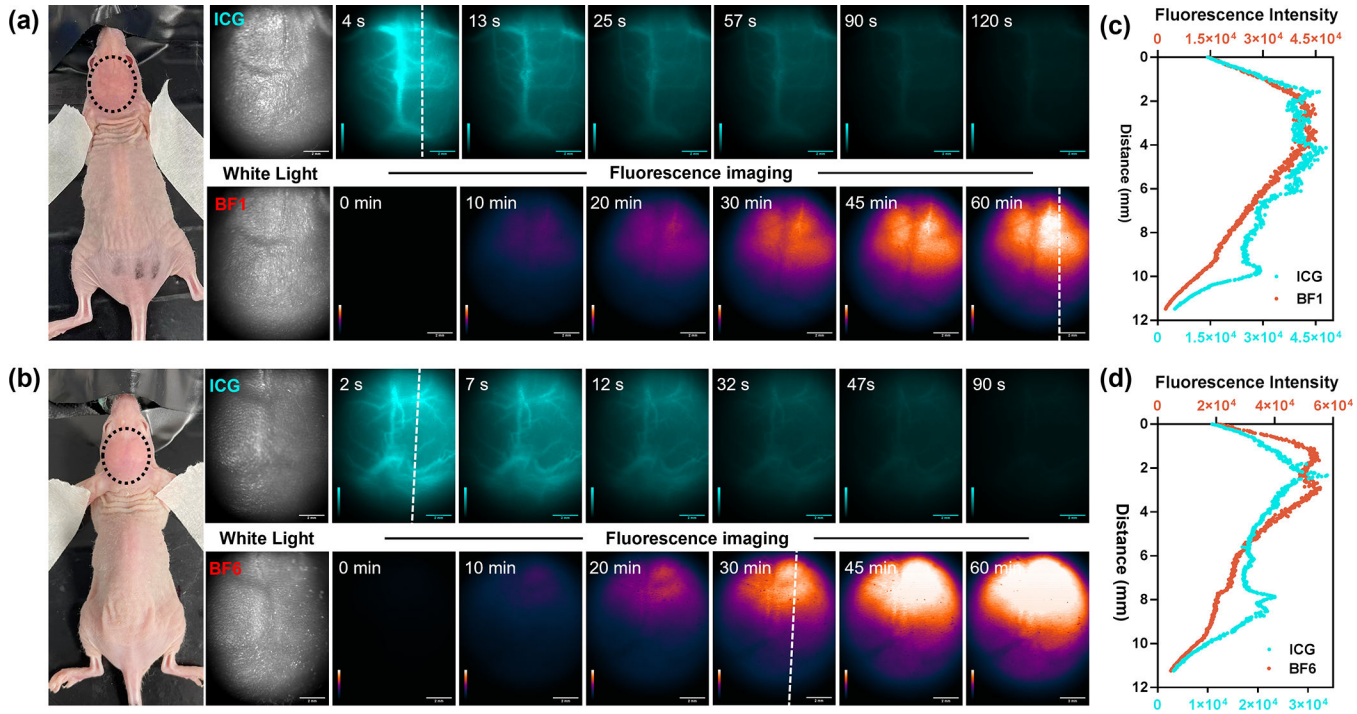

Figure 4.

(a) White light and noninvasively *in vivo* NIR-II fluorescence imaging of mouse brains bearing primary glioma tumor after treating ICG and **BF1** (200 μM, 200 uL, tail vein injection) at six time points (4, 13, 25, 57, 90, 120 s for ICG; 0, 10, 20, 30, 45, 60 min for **BF1**). **(b)** White light and noninvasively *in vivo* NIR-II fluorescence imaging of mouse brains bearing primary glioma tumor after treating ICG and **BF6** (200 μM, 200 uL, tail vein injection) at six time points (2, 7, 12, 32, 47, 90 s for ICG; 0, 10, 20, 30, 45, 60 min for **BF6**), respectively. The laser power was 70 mW cm^{-2}, 808 nm laser, 1000 nm LP filter; **(c, d)** Cross-sectional fluorescence intensity profile along the white dash lines in **(a)** and **(b)** collected by 1000 nm long-pass filter.

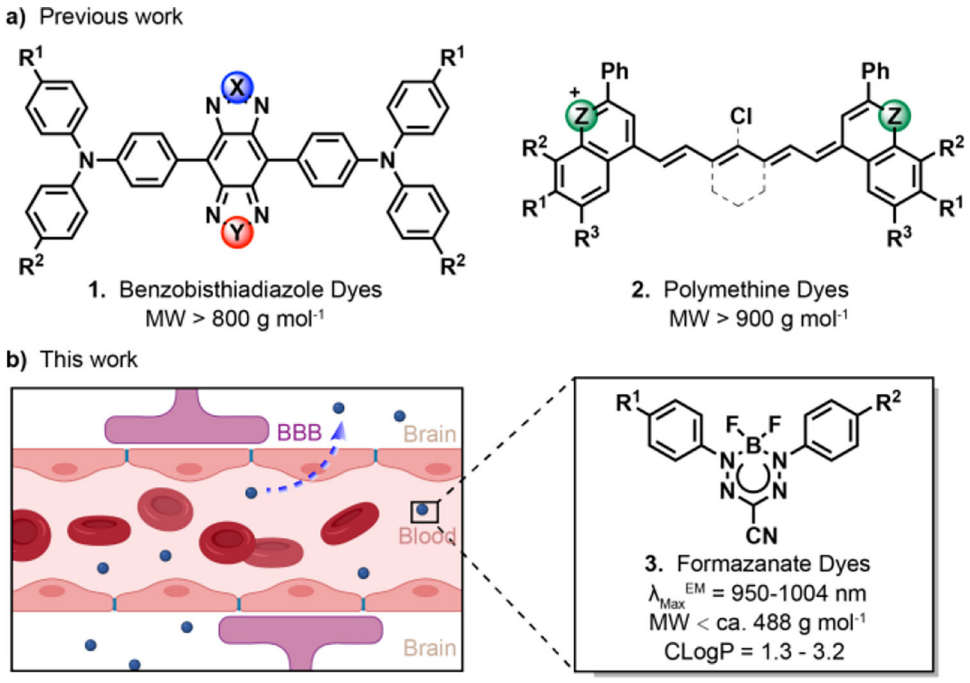

Scheme 1.

Small-molecule scaffolds with NIR-II fluorescence. **(a)** Previous molecules which possess NIR-II fluorescence. **(b)** The schematic diagram of BF_2 formazanate dyes penetrating the BBB from the circulation.